Experimental and Numerical Analysis of Shell-and-Tube Heat Exchangers for Heat Transfer Education

GUESSAB AHMED, AIT AMRANE OUARDIA
Department of Mechanical Engineering, National Polytechnic School of Oran,
1523 EL M'Naouar Es-Senia Oran,
ALGERIA

Abstract: - The present study investigates heat transfer in a small parallel-flow shell-and-tube heat exchanger through experimental and numerical approaches. Experimental measurements were carried out on a dedicated test bench. The three-dimensional flow is modeled using the incompressible, single-phase Navier–Stokes and energy equations. For the discretization of the transport equations, we used the ANSYS Fluent 2025 calculation code, specifically the student version, which employs the finite volume method. In this work, we simulated different configurations, choosing three flow rates for the hot fluid (V_h = 1.4, 2, 2.5 L/min) and a fixed flow rate of 1.4 L/min for the cold fluid in all three cases. The simulation results closely match the experimental results. Increasing the hot water flow rate improves heat transfer between the two fluids, consequently enhancing and increasing the overall thermal efficiency. This study aims to consolidate our students' knowledge of the numerical analysis of a shell-and-tube heat exchanger, compare the results with experimental data, and perform visualization analyses of the flow within the tubes and the shell. Correlation-based methods can signal the presence of a design flaw, but CFD simulations are also capable of determining the origin and location of that flaw.

Keywords: - CFD; Experimental validation; Heat transfer; Shell-and-tube heat exchanger; Flow visualization; Thermal efficiency; ANSYS Fluent.

Received: April 5, 2026. Revised: May 19, 2026. Accepted: June 21, 2026. Published: November 13, 2026.

1 Introduction

Most heat transfer in industrial applications employs non-contact heat transfer between fluids, which can achieve high efficiency for various applications [1], [2].

In refinery and petroleum processing industries, for instance, separation and reaction units require precise thermal control to establish temperature gradients and reach reaction threshold conditions. Several types of heat exchangers exist in the industry, but shell-and-tube heat exchangers constitute around 40% due to their robustness, ease of maintenance, and capacity [3], [4], [5], [6]. In particular, investigations of parallel-flow arrangements have shown that increasing the hot-fluid volumetric flow rate enhances heat transfer rates while inducing higher pressure drops on the shell side [7], [8]. Some studies in the literature focus on the operating mode of shell-and-tube heat exchangers. For example, reference [9] studied the impact of inlet flow rates on heat transfer coefficients, showing a remarkable improvement in performance with increasing hot liquid flow rates. Reference [10] investigated a multi-passage concept for improving the thermal performance of water–air cross-flow tube-and-fin heat exchangers by dividing the water flow into several passages. The results showed that the thermal performance increases rapidly at low water flow rates but becomes nearly constant at high flow rates. The proposed multi-passage configuration increased the overall thermal performance by up to 25.7%, with greater enhancement at higher air velocities and lower water flow rates. In addition, the configuration reduced the water-side pressure drop by up to 40.6%, demonstrating its potential for simultaneously improving heat-transfer performance and hydraulic efficiency.

Despite these advances, limited research has addressed the combined use of experimentally validated CFD models and small-scale shell-and-tube heat exchangers as a research-based

framework for analyzing heat transfer phenomena under controlled operating conditions, particularly in configurations suitable for laboratory-scale systems. Moreover, the potential of such validated models to support quantitative analysis and learning-driven exploration of thermal–fluid behavior remains underexplored.

This work combines experimental investigations and numerical calculations to analyze heat transfer and fluid behavior in a small-scale shell-and-tube heat exchanger. This study aims to observe the effect of variations in the hot water volumetric flow rate on the performance of this type of exchanger. The work will proceed as follows: first, experimental measurements will be performed on a test bench; second, SolidWorks software will be used for the design and dimensioning of the exchanger component by component; third, the fluids and solids within the exchanger will be modeled and simulated using the ANSYS Fluent CFD software [11].

Finally, before interpreting the results, the numerical model must be validated. To this end, this study will examine the mesh independence and then compare the numerical results with the experimental results.

By bridging theoretical analysis, experimental observation, and numerical simulation, this work contributes to both heat exchanger research and the advancement of evidence-based instructional approaches in thermal and fluid engineering.

2. Description of the Test Bench

A process diagram of the experimental setup is presented in Figure 1. The miniature heat exchanger simulated in this study illustrates water-to-water heat transfer in a shell-and-tube heat exchanger. The heat exchanger contains a shell and seven tubes that have four transverse baffles. The schematic diagram of the heat exchanger is presented in Figure 2. In normal operation, hot fluid from the hot water tank enters the manifold at one end of the shell and passes through the stainless-steel tube bundle, while cold fluid from the cold-water supply passes through the shell. The technical characteristics and operating configuration of the experimental test bench were obtained from the manufacturer's documentation [12].

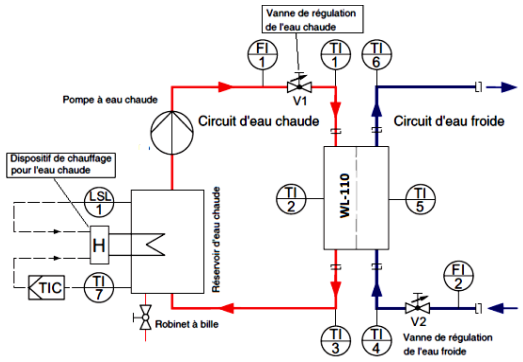


Fig. 1: Process diagram of experimental setup
Source: [12]

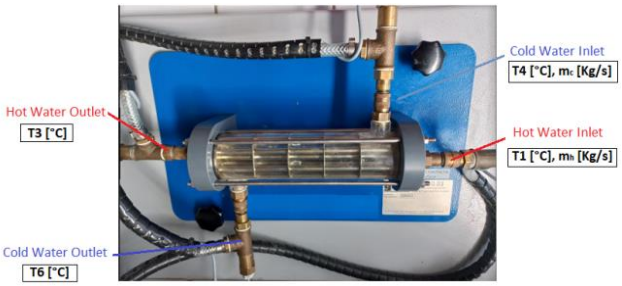


Fig. 2: Schematic diagram of the heat exchanger to be investigated connected to the supply unit
Source: [12]

The heat exchanger is connected to a service unit (Figure 3).



Fig. 3: Photo of a miniature shell-and-tube heat exchanger (test bench)
Source: [12]

The technical and geometrical details of the heat exchanger model are presented in Table 1.

Table 1. Constant design parameters and geometric parameters of the shell-and-tube heat exchanger

Parameters	Value
Number of shell passes	1
Shell inner diameter, $D_{shell,I}$ (mm)	44
Shell inner diameter, $D_{shell,o}$ (mm)	50
Tube inner diameter, $d_{tube,I}$ (mm)	4
Tube outer diameter, $d_{tube,o}$ (mm)	6
Nozzle diameter D_{nozzle} (mm)	14
Nozzle length, L_{nozzle} (mm)	12
Baffle thickness (mm)	1
Heat exchanger length (mm)	184
Tube pitch (mm)	12
Tube pitch angle (mm)	14.5
Baffle spacing (mm)	37
Number baffle spacing zones	4
Number of tubes in bundle	7
Heat transfer area (m^2)	0.02
Number of shell passes	1

Source : [12]

The exchanger shell was fabricated from Plexiglas to allow visual observation of the flow behavior, as illustrated in Figure 2. A proportional–integral–derivative (PID) controller was used to regulate the inlet temperature of the hot water supplied to the tube side. The volumetric flow rates were measured using paddle-wheel flow meters with a measurement range of 0.33–4.17 L/min and an accuracy of ±2% of full scale. All measuring instruments were calibrated prior to the experimental runs to ensure data reliability. A total of nine experimental operating conditions, summarized in Table 2, were examined.

Table 2. Boundary conditions applied at the inlet tube and inlet shell faces

Cases	Rate of volume flow in tube side V_h [L/min]	Rate of volume flow in shell side V_c [L/min]
T7 = 50°C	1.4	1.4
	2.0	
	2.5	
T7 = 60°C	1.4	1.4
	2.0	
	2.5	
T7 = 70 °C	1.4	1.4
	2.0	
	2.5	

Source: Created by the authors.

The heat exchanger test bench comprises:

- A structure made of stainless steel AISI 304, mounted on wheels;
- A variable area flowmeter for hot water and a variable area flowmeter for cold water;
- four resistance temperature sensors with digital displays:
  - T1: inlet temperature of hot water;
  - T3: outlet temperature of hot water;
  - T4: inlet temperature of cold water;
  - T6: outlet temperature of cold water;
- An emergency stop button.

3. Mathematical Formulation

3.1 Geometrical configuration

The primary objective of this study was to investigate the thermal and hydraulic performance of a shell-and-tube heat exchanger model (Figure 4) while simultaneously providing a practical learning framework for engineering education. In this simulation, two liquids at different temperatures pass through the exchanger; the first liquid flows through the shell side, as shown in Figure 5, while the other flows through the tubes (Figure 6). The heat exchanger consists of a bundle of seven stainless steel tubes and four baffles. The distribution and position of these baffles within the shell allow a fluid passage of approximately 15% of the total cross-section (Figure 7). All dimensions are given in Table 1.

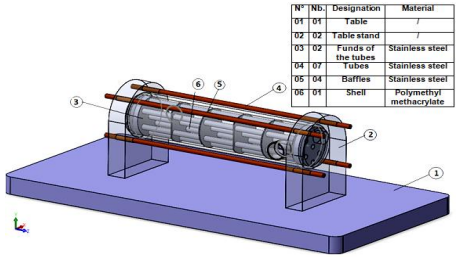


Fig. 4: Assembly drawing of a shell and tube heat exchanger (isometric view)
Source: Created by the authors

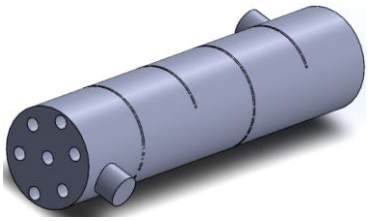


Fig. 5: Shell Fluid domain 1: Cold water
Source: Created by the authors.

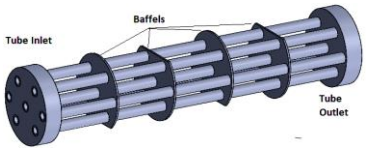


Fig. 6: Tubes and 4 baffles (Fluid domain 2: Hot water)
Source: Created by the authors.

Four return plates (baffles) were used to divide the shell-side flow path, deflecting cold water to promote heat transfer. This arrangement produces a partially cross-flow pattern, enabling students to observe and analyze complex flow behavior and its effect on thermal performance. Based on the experimental model, a proportionally scaled numerical model was developed for CFD simulations.

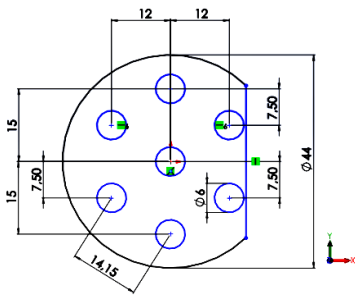


Fig. 7: Geometric parameters of the Baffles
Source: Created by the authors.

3.2 Governing equation (Laminar)

The configuration obtained during the experimental setup in the test bench showed that the flow was considered steady, and after Reynolds number calculations, the flow in this small exchanger was laminar (see Tables 6 and 7, page 8). Gravitational effects were neglected, and no mass or momentum transfer was assumed at the fluid interfaces. Water was used as the working fluid in both the shell and the tubes. The FLUENT materials database was used to define materials in the solver. The analyses were primarily based on water as the main material. Its properties were redefined using piecewise linear functions. Equations 1 through 5 were redefined to determine the density, thermal conductivity, viscosity, and specific heat capacity of water [11].

$$\mu(T) = 10^{-4}\left(0.002T^2 - 0.3389T + 17.199\right) \quad (1)$$

$$\rho(T) = -0.0038T^2 - 0.0505T + 1002 \quad (2)$$

$$\lambda(T) = -9.87\times10^{-6}T^2 + 2.238\times10^{-3} + 0.5536 \quad (3)$$

$$C_p = 4180 \quad (4)$$

$$\Pr(T) = 1.577\times10^{-3}\,T^2 - 0.261\,T + 12.501 \quad (5)$$

The averaged equations that describe this type of flow and the heat transfer are as follows:

$$\nabla.\vec{U} = 0 \quad (6)$$

$$\nabla.\left(\rho\vec{U}\vec{U}\right) = -\nabla p + \nabla\left[\mu\left(\nabla\vec{U} + (\nabla U)^T\right)\right] \quad (7)$$

$$\nabla.\left(\vec{U}(\rho E + p)\right) = \nabla.\left(\lambda_{eff}\nabla T\right) \quad (8)$$

Where: $\vec{U}$ is the velocity vector, μ is the dynamic viscosity, ρ is the density, p is the static, E: total energy ($E = h - \frac{p}{\rho} + \frac{U^2}{2}$), h is the sensible enthalpy, and λ_{eff} effective thermal conductivity
The log-mean temperature difference (LMTD) method is used to calculate the actual heat transfer rate (Q). Combined with the NTU approach, it allows theoretical predictions to be linked to experimental results.

Analytical calculations

Hot fluid:

$$Q = \rho_h \overset{*}{V}_h c_{p,h}\left(T_1 - T_3\right) \quad (9)$$

Cold fluid:

$$Q = \rho_c \overset{*}{V}_c c_{p,c} (T_6 - T_4) \quad (10)$$

And

$$Q = Q_h = Q_c \quad (11)$$

Heat capacity of fluids:

$$C_h = \rho_h \overset{*}{V}_h c_{p,h} \quad (12)$$

$$C_c = \rho_c \overset{*}{V}_c c_{p,c} \quad (13)$$

These terms are essential for the analysis (NTU method)

Heat transfer rate:

$$Q = K_m A_m \Delta T_{lm} \quad (14)$$

The logarithmic mean temperature difference is calculated using the following expression, [4], [13], [14]:

$$\Delta T_{LM} = \frac{\Delta T_{\max} - \Delta T_{\min}}{\ln(\Delta T_{\max} / \Delta T_{\min})} \quad (15)$$

Temperature differences for the parallel flow are described briefly in the following equations:

$$\Delta T_{\max.} = T_1 - T_4 \quad (16)$$

$$\Delta T_{\min.} = T_3 - T_6 \quad (17)$$

The average heat transmission coefficient (k_m) is defined as

$$K_m = \frac{C_{p,c} \cdot \rho_c \overset{*}{V}_c (T_6 - T_4) - C_{p,h} \rho_h \overset{*}{V}_h (T_3 - T_1)}{2 A_m \Delta T_{LM}} \quad (18)$$

$$A_m = \frac{A_h - A_c}{\ln(A_h / A_c)} \quad (19)$$

The Nusselt number is a dimensionless number that describes how heat moves between the fluid inside a tube and the outside of the tube (shell). The Nusselt number is calculated using the following correlations [15]:

$$Nu = \frac{hd}{\lambda} \quad (20)$$

3.3 Mesh details

Mesh generation of the heat exchanger is performed using ANSYS Gambit (v. 2.4.6) [16] as shown in Figure 8 and Figure 9. The shell surface, which is perpendicular to the tubes, and the baffles are meshed; then the tube surfaces are meshed accordingly. Similarly, the nozzle inlets and the nozzle side are meshed, and then the outer surface of the shell is meshed correspondingly. After all the surfaces are meshed successfully, the shell volume is meshed. Then, the tube volume is meshed. The meshing procedure is similar to the process explained above.

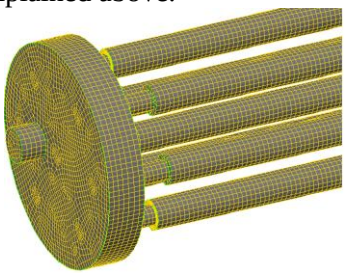


Fig. 8: Tubes mesh
Source: Created by the authors.

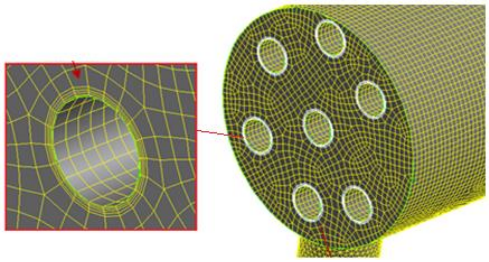


Fig. 9: Part of the fluid volume and the mesh structure in the shell
Source: Created by the authors.

3.4 Modeling choices

In the current model, on both the shell and tube sides, the flow is laminar. Therefore, the laminar viscous model is employed. First-order discretization is employed for the pressure, momentum, and energy equations. The convergence criterion of the pressure residual is set to 10^{-6}, and for all other residuals it is set to 10^{-3}.

3.5 Boundary conditions

The boundary conditions applied in the numerical model were as follows:

- All heat exchanger walls, including the baffles, were modelled as three-dimensional shells, which required special boundary conditions for both the flow and heat transfer equations.
- Interior wall boundary conditions were applied to account for the separation of fluids by the baffles on both sides.
- Hot water entered the tube side at a specified volume flow rate (V_h) and inlet temperature (T1).

- Cold water entered the shell side at a volume flow rate (V_c) and inlet temperature (T4).
- All other exterior boundaries were considered thermally insulated.

3.6 Mesh optimization

The objective of the mesh optimization study was to determine a suitable mesh with the minimum number of nodes for which the simulation results remain unchanged upon further refinement. To this end, six meshes with varying node counts were generated and tested. The outlet temperature of the hot water was then compared for each mesh (see Figure 10). The results indicate that the outlet temperature increased with the number of nodes until it stabilized at a mesh containing 25,363 nodes. Consequently, mesh 5, with 25,363 nodes, was selected for all simulations conducted in this study.

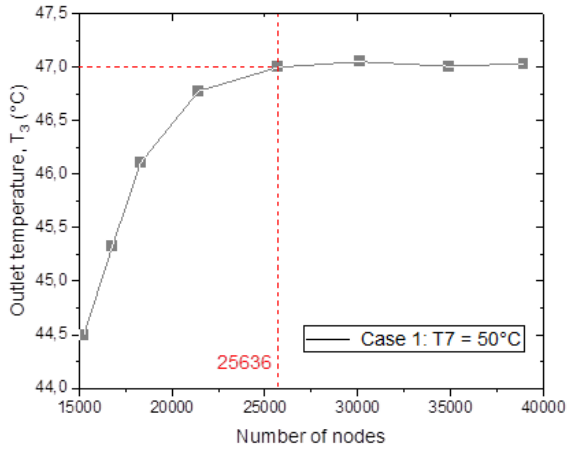


Fig. 10: Mesh independence study of outlet temperature
Source: Created by the authors.

4. Results

4.1 Experimental results

Direct measurement at the terminals of the heat exchanger involves performing a heat balance by recording the inlet and outlet temperatures of both fluids, as well as measuring their volumetric flow rates. The experiments described here were conducted on a parallel-flow shell-and-tube heat exchanger. The hot water inlet temperature, T7 (monitored by a temperature controller), was recorded to ensure accurate evaluation of the actual operating conditions, while the cold-water inlet temperature, T4, was used for comparison and validation purposes. Using Equations (9) to (20), the results were organized into Tables 3 and 4. Table 3 summarizes the inlet and outlet temperatures for various hot water volume flow rates, while the shell-side flow rate was maintained constant at 1.4 L/min for all cases. Table 4 presents the relationship between the average heat transfer coefficient (K_m) and the volumetric flow rate of hot water. The results indicate that the fluid with the smallest specific heat capacity, cold water in the shell, undergoes the largest temperature change.

Table 3. Experimental inlet and outlet temperatures

Cases	V_h (L/min)	T1 (°C)	T3 (°C)	T4 (°C)	T6 (°C)
T7 = 50°C	1.4	52.0	47.0	25.8	31.0
	2.0	50.8	46.8	25.6	31.3
	2.5	51.4	47.7	25.7	32.2
T7 = 60°C	1.4	63.0	55.1	25.8	33.2
	2.0	60.6	54.1	26.0	33.5
	2.5	61.3	55.7	25.7	34.7
T7 = 70 °C	1.4	70.0	60.3	26.0	35.0
	2.0	70.0	61.7	26.0	36.3
	2.5	71.0	63.3	25.8	37.5

Volumetric Flow of a fluid in a shell, V_c = 1.4 (L/min)

Source: Created by the authors.

Table 4. Experimental results

Cases	V_h (L/min)	dQm/dt (kW)	ΔTLM	K_m (kW/m^2.K)
T7 = 50°C	1.4	0.489	20.74	1.1749
	2.0	0.552	19.95	1.370
	2.5	0.634	20.17	1.5663
T7 = 60 °C	1.4	0.738	28.87	1.274
	2.0	0.814	27.04	1.5015
	2.5	0.9167	27.66	1.6515
T7 = 70 °C	1.4	0.8912	33.71	1.3174
	2.0	1.051	33.77	1.551
	2.5	1.2158	34.56	1.7533

Source: Created by the authors.

Figure 11, Figure 12 and Figure 13 illustrate the temporal evolution of temperatures T_1, T_3, T_4, and T_6, as well as the volumetric flow rates dV1/dt and dV2/dt. The experiment was initiated to stabilize the process, following the operating instructions provided with the test bench to obtain more reliable results. Numerical calculations indicate that the flow regime is steady and stable. These figures illustrate the temporal evolution of temperatures and volumetric deflections for both hot and cold fluids at the inlet and outlet of the tubes and the heat exchanger shell. The heat transfer process begins and occurs progressively as the hot water flow rate increases from 1.4 L/min to 2.5 L/min. This process is repeated, again waiting for system stability, and finally the flow rate is increased to 2.5 L/min. This procedure is described in the test bench user manual to ensure the stability and reliability of the experimental data.

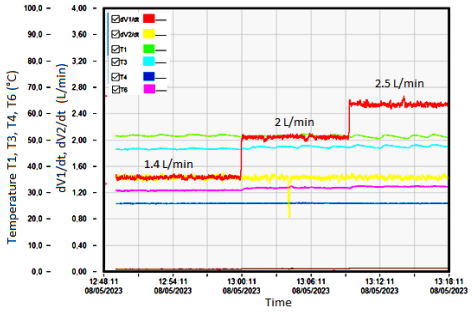


Fig. 11: Temporal evolution of temperature and volumetric flow rate (T7 = 50°C)
Source: Created by the authors.

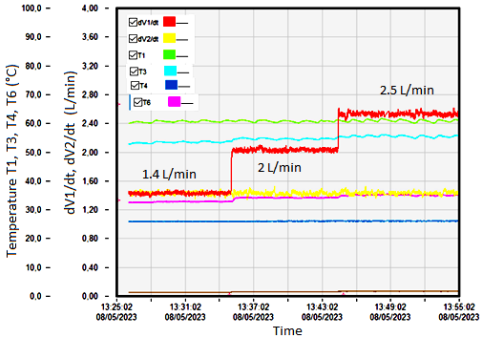


Fig. 12: Temporal evolution of temperature and volumetric flow rate (T7 = 60°C)
Source: Created by the authors.

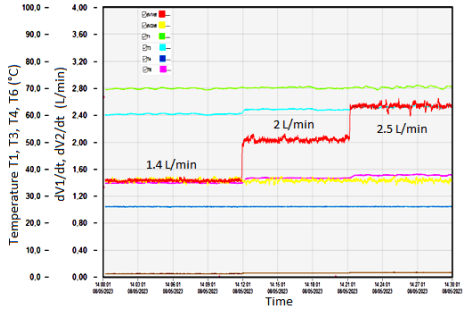


Fig. 13: Temporal evolution of temperature and volumetric flow rate (T7 = 70°C)
Source: Created by the authors.

4.2 CFD analysis

Within the framework of the CFD simulations of this exchanger, three operating cases are studied, representing a total of nine numerical simulations**.** Table 5 groups together the three simulation cases and the results obtained during these numerical simulations. The results indicate that the total heat transfer coefficient increases when the hot water flow rate is increased. In Figure 14, Figure 15 and Figure 16, the numerical calculations show that

when the hot water flow rate increases from 1.4 L/min to 2.5 L/min, the heat transfer coefficient (k_m) increases by approximately 36.4%, 32.2%, and 36.4% for the cases T7 = 50°C, 60°C, and 70°C, respectively. For the experimentally obtained data, the overall heat transfer coefficient varies by 33.3%, 29.6%, and 33.1% for the same cases, respectively. The operating conditions are identical. The discrepancy between the simulation predictions and the experimental results is low, around 8.5%, which shows that the numerical model is well calibrated compared to experiments. Therefore, it is possible to analyze all the other characteristics of our heat exchanger. Figure 14, Figure 15 and Figure 16 illustrate the influence of hot fluid volume flow rate in the tube side on the average heat transfer coefficient (k_m). The results show that increasing the hot-side flow rate leads to higher average heat transfer coefficients. Additionally, the impact of the hot fluid's inlet temperature becomes more pronounced at higher tube-side flow rates. The percentage error between the analytical calculations and the CFD analysis ranged from 5.7% to 8.5%, indicating that the boundary conditions and model assumptions were appropriate for simulating variations in operating conditions.

Table 5. Results of the CFD analysis and the analytical calculations (Experimental)

Cases	V_h [L/min]	Heat Transfer Coeff. k_m [kW/m^2. K]		
		Exp.	CFD	Err. %
T7 = 50 °C	1.4	1,1749	1,0749	8.511
	2.0	1,3789	1,2789	7,251
	2.5	1,5663	1,4663	6,384
T7 = 60 °C	1.4	1,2739	1,1739	7,849
	2.0	1,5015	1,4015	6,659
	2.5	1,6515	1,5515	6,055
T7 = 70 °C	1.4	1,3174	1,2117	7,590
	2.0	1,5509	1,4509	6,447
	2.5	1,7533	1,6533	5,703

Source: Created by the authors.

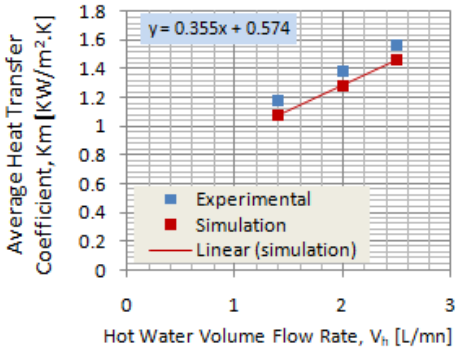


Fig. 14: Heat transfer coefficient, K_m (T_7 = 50°C)
Source: Created by the authors.

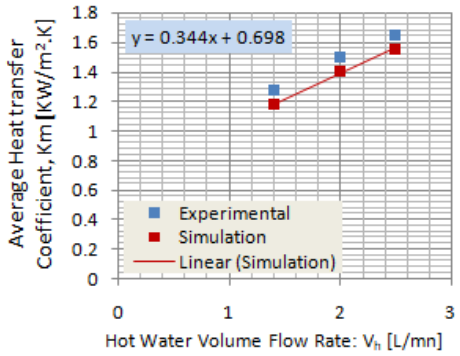


Fig. 15: Heat transfer coefficient, K_m (T_7 = 60°C)
Source: Created by the authors.

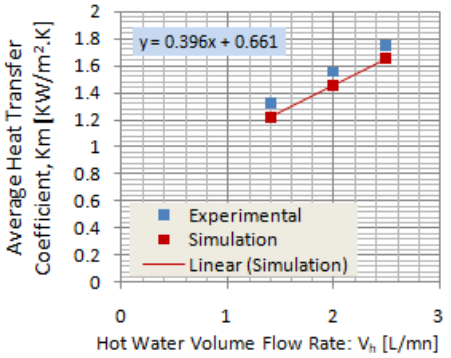


Fig. 16: Heat transfer coefficient, K_m (T_7 = 70°C)
Source: Created by the authors.

The thermal efficiency of the hot side is defined analogously to the heat exchanger effectiveness, that is, as the ratio of the actual temperature drop of the hot fluid to the maximum possible temperature difference between the hot and cold fluids [17], [18].
The hot-side thermal efficiency is defined as follows:

$$\eta_{hot} = \frac{T_1 - T_3}{T_1 - T_4} \quad (21)$$

Similarly, the thermal efficiency of the cold side (η_{cold}) is defined as follows:

$$\eta_{cold} = \frac{T_6 - T_4}{T_1 - T_4} \quad (22)$$

The variation in overall heat exchange efficiency of the fluid with hot-water flow is shown in Figure 17. It is clear that the overall heat exchange efficiency decreases as the flow rate increases. Figure 18 shows the effect of cold-water flow on the thermal efficiency of the shell-side fluid (η_{cold}), showing that η_{cold} increases with higher tube-side flow rates. These observations provide an opportunity for students to understand the trade-offs in heat exchanger operation.

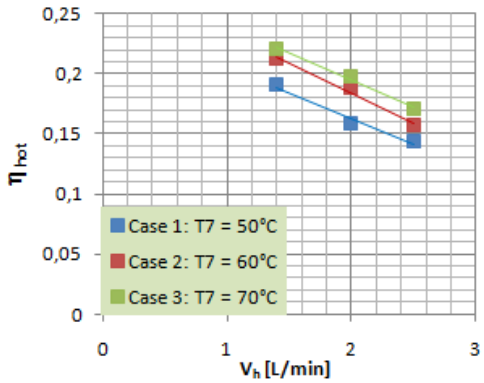


Fig. 17: Thermal efficiency of hot water
Source: Created by the authors.

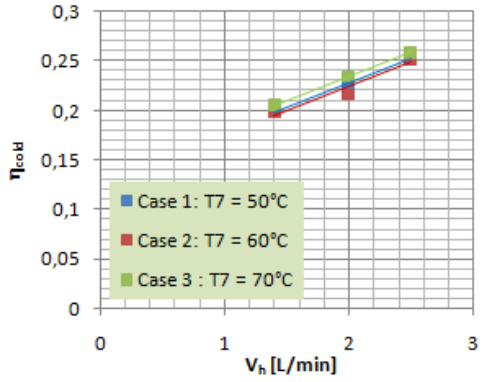


Fig. 18: Thermal efficiency of cold water
Source: Created by the authors.

The influence of the hot water volumetric flow rate on the performance of a shell-and-tube heat exchanger was investigated by calculating the Nusselt numbers (Nu_{Tube}, Nu_{Shell}). The CFD analysis was validated by comparison with analytical calculations, as summarized in Tables 6 and 7.

Table 6. The CFD analysis and the analytical calculations (AC)

Cases	Re_{tube}	Nu_{tube}		
		Exp.	CFD	Err. %
T7 = 50 °C	271,89	5,148	4,988	3,114
	383,70	5,798	5,599	3,448
	485,56	6,242	6,011	3,713
T7 = 60 °C	315,29	5,111	4,610	9,809
	438,74	5,764	5,223	9,389
	558,45	6,205	5,814	6,300
T7 = 70 °C	343,32	5,091	4,665	8,357
	495,99	5,629	5,168	8,188
	631,30	6,170	5,558	9,922

Source: Created by the authors.

Table 7. The CFD analysis and the analytical calculations (AC)

Cases	Re_{shell}	Nu_{shell}		
		AC	CFD	Err. %
T7 = 50 °C	1012,32	28,65	28,60	0,17
	1014,74	28,66	28,612	0,17
	1025,78	28,71	28,665	0,17
T7 = 60 °C	1048,62	28,82	28,806	0,04
	1052,00	28,84	28,824	0,05
	1055,16	28,85	28,84	0,06
T7 = 70 °C	1055,16	28,88	28,84	0,13
	1073,81	28,946	28,91	0,12
	1084,75	29,000	28,947	0,17

Source: Created by the authors.

The Nusselt number, analyzed as a function of the volumetric flow rates on the tube side, is shown in Figure 19, Figure 20 and Figure 21. These figures show the variation of the Nusselt number (Nu_{tube}) as a function of the Reynolds number calculated in the tubes (Retube). By varying the volumetric flow rate of the hot water, the flow was observed to be laminar. Equation 23 [19] was used for the Nusselt number calculations.

$$Nu_{tube} = 1.86\left(\frac{d_i}{L_t}\mathrm{Re.Pr}\right)^{1/3}\left(\frac{\mu_b}{\mu_w}\right)^{0.14} \quad (23)$$

$(0.48 < Pr < 16.7$ and $0.0044 < \mu/\mu_w < 9.75)$

The subscript "b" means that this quantity must be calculated at the average temperature of the fluid; then, the subscript "w" indicates that it denotes the value at the temperature of the solid wall.

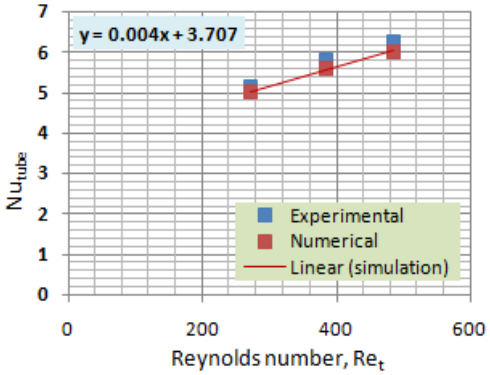


Fig. 19: The variation of the Nusselt number with the Reynolds number for the tube within the heat exchanger (Case 1: T7 = 50°C)
Source: Created by the authors.

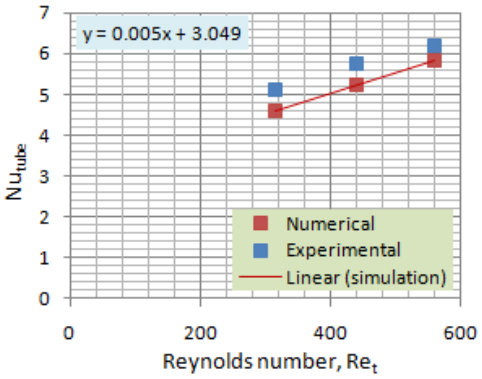


Fig. 20: The variation in Nusselt number with Reynolds number for the tube in the heat exchanger (Case 2: T7 = 60°C)
Source: Created by the authors.

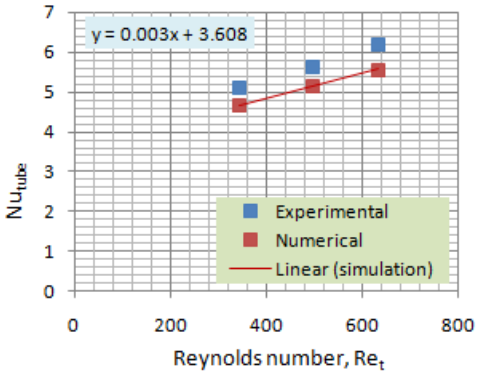


Fig. 21: The variation in the Nusselt number with respect to the Reynolds number of the tube in the heat exchanger (Case 3: T7 = 70°C)
Source: Created by the authors.

The Nusselt number [20], [21], is analyzed as a function of the shell-side volumetric flow rates and is illustrated in Figure 22, Figure 23 and Figure 24.

$$Nu_{shell} = 0.36\left(\mathrm{Re}_{shell}\right)^{0.55}\left(\mathrm{Pr}_{shell}\right)^{0.33} \quad (24)$$

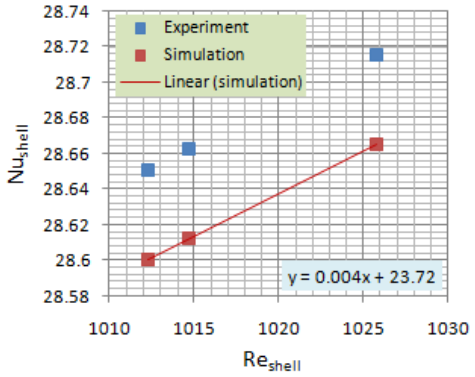


Fig. 22: Nusselt number versus Reynolds number of the shell in the heat exchanger (Case 1)
Source: Created by the authors.

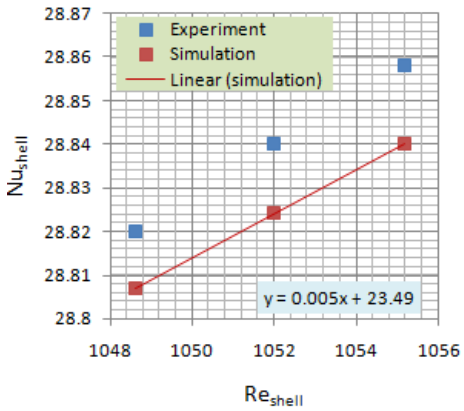


Fig. 23: Nusselt number versus Reynolds number of the shell in a heat exchanger (Case 2)
Source: Created by the authors.

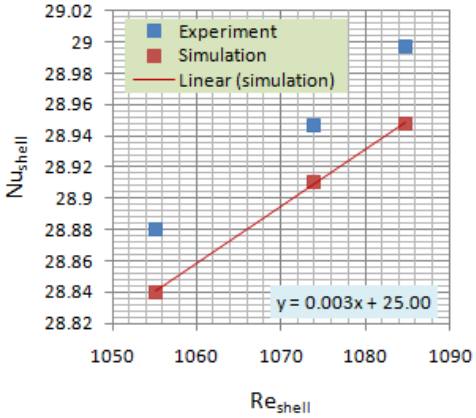


Fig. 24: Nusselt number versus Reynolds number of the shell in a heat exchanger (Case 3)
Source: Created by the authors.

The pressure drop in pipes is generally influenced by several geometric factors and fluid properties. This pressure drop is due to auxiliary friction losses. The tube-side pressure drop can be calculated using the following Equation 25 [6]. The variations in tube-side pressure drop for the three operating cases are presented in Figure 25, Figure 26 and Figure 27. Analyzing the tube-side pressure drop provides students with insights into the interplay between flow characteristics, geometry, and fluid properties, reinforcing fundamental principles of fluid mechanics and thermodynamics while emphasizing the balance between thermal performance and hydraulic constraints in heat exchanger design.

$$\Delta P_{tube} = 2\left(\frac{f\,..L_t}{d_i}+1\right)N_p \rho V^2 \quad (25)$$

$$f = 16/\mathrm{Re}_t \quad (26)$$

$$\mathrm{Re}_t = \frac{\rho U_m D_i}{\mu} \quad (27)$$

where ΔP_{tube} is the pressure drop on the tube side, Re_t is the Reynolds number in the tube, and f is the friction factor.
The tube-side pressure drop in the shell-and-tube heat exchanger is summarized in Table 8. The difference between the two calculations, CFD and experimental, was 9.48% for case 1, 21% for case 2, and 10.5% for case 3. These results show a difference between the two approaches.

Table 8. Tube-side pressure drops: The CFD analysis and the analytical calculations (Exp.)

T7	Reynolds Number (Re_t)	Tube-side Pressure Drop [Pa]		
		Exp.	CFD	Err. %
50	271,89	10,541	11,541	9,486
°C	383,70	16,914	17,914	5,912
	485,56	22,777	23,777	4,390
60	315,29	9,423	11,411	21,09
°C	438,74	15,456	17,423	12,723
	558,45	20,895	22,899	9,60
70	343,32	8,856	10,356	16,93
°C	495,99	14,275	15,775	10,507
	631,30	19,433	20,933	7,718

Source: Created by the authors.

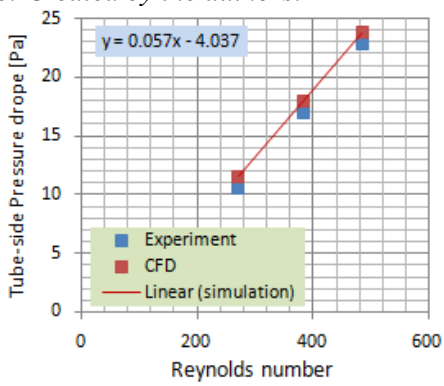


Fig. 25**:** Tube-side pressure drop, (ΔP) (T7 = 50°C). *Source: Created by the authors.*

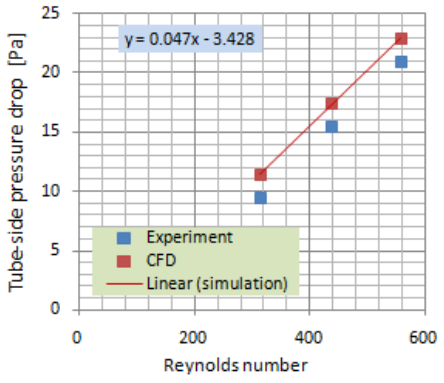


Fig. 26: Tube-side pressure drop, (ΔP) (T7 = 60°C) *Source: Created by the authors.*

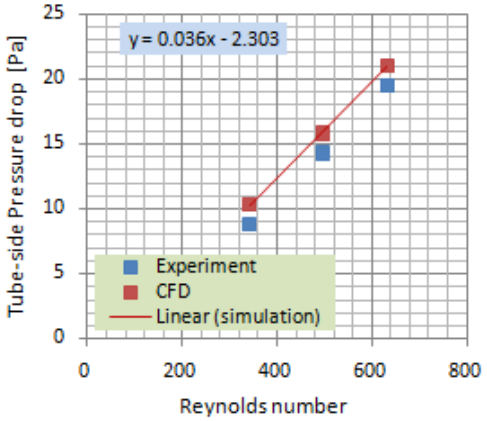


Fig. 27**:** Tube-side pressure drops (ΔP) (T7 = 70°C) *Source: Created by the authors.*

The shell-side pressure drop can be calculated using the following equation, with the results summarized in Table 9 [20], [21], [22]:

$$\Delta P_{shell} = f \frac{D_S}{D_E} 4\left(N_b + 1\right)\frac{\rho V^2}{2} \quad (28)$$

$$f = \exp\left(0.576 - 0.19\ln\left(\mathrm{Re}_s\right)\right) \quad (29)$$

$$D_E = 4\left(\frac{\sqrt{3}P_t^2}{4} - \frac{\pi d_0^2}{8}\right)/\frac{\pi d_0}{2} \quad (30)$$

$$\mathrm{Re}\,s = \frac{\rho U_m D_e}{\mu} \quad (31)$$

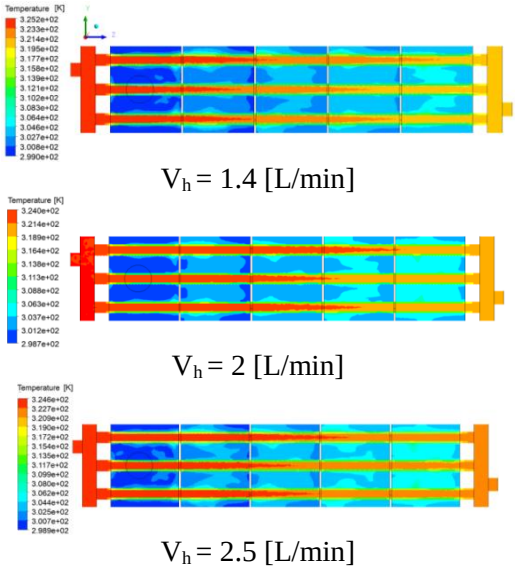
Where: ΔP_{shell} = pressure drop, $\mathrm{Re}_{\mathrm{Shell}}$ = Reynolds number, f = friction factor, P_t = tube pitch.

Table 9. Pressure drops in the shell side: comparison of the CFD analysis with the analytical calculations (experimental)

Cases	Reynolds Number ($\mathrm{Re}_{\mathrm{shell}}$)	Pressure Drop in shell side {Pa}		
		Exp.	CFD	Err. %
T7 = 50 °C	1012.31	3.361	3.473	3.33
	1014.74	3.359	3.471	3.33
	1025.78	3.352	3.464	3.34
T7 = 60 °C	1055.37	3.333	3.445	3.36
	1048.64	3.337	3.449	3.35
	1055.16	3.333	3.449	3.36
T7 = 70 °C	1048.46	3.336	3.448	3.35
	1073.81	3.321	3.432	3.37
	1084.75	3.313	3.428	3.8

Source: Created by the authors.

A flat plane was created along the flow direction at the mid-section of the shell-and-tube heat exchanger to analyze the temperature distribution. Figure 28, Figure 29 and Figure 30 show the temperature contours on the longitudinal cross-section of the heat exchanger for the three case studies. The volumetric flow rate of the hot fluid has a clear influence on the temperature distribution.

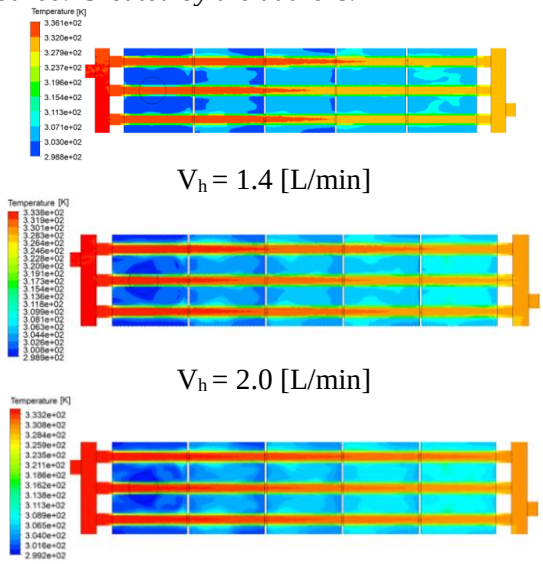


V_h = 1.4 [L/min]

V_h = 2 [L/min]

V_h = 2.5 [L/min]

Fig. 28**:** Temperature distribution (T_7 = 50°C) *Source: Created by the authors.*

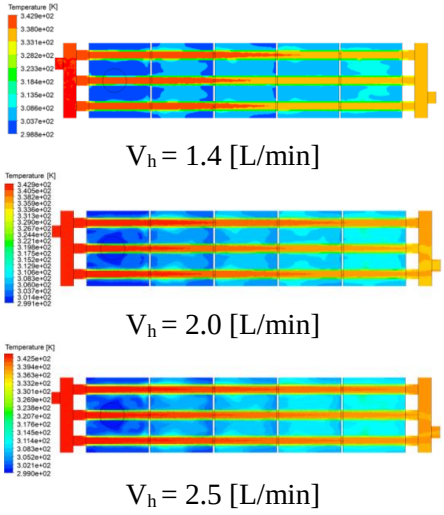


V_h = 1.4 [L/min]

V_h = 2.0 [L/min]

V_h = 2.5 [L/min]

Fig. 29: Temperature distribution (T_7 = 60°C) *Source: Created by the authors.*



V_h = 1.4 [L/min]

V_h = 2.0 [L/min]

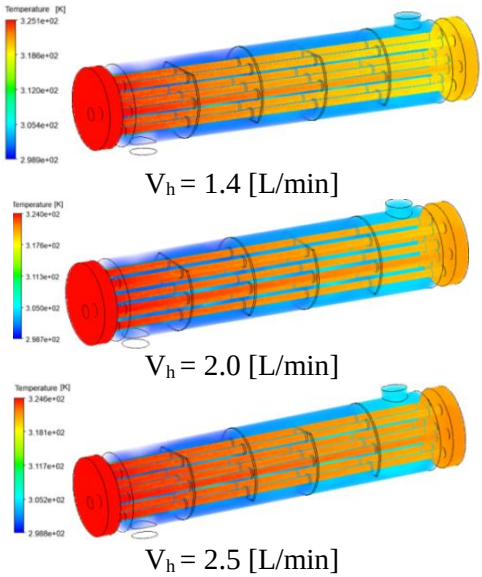
V_h = 2.5 [L/min]

Fig. 30**:** Temperature distribution (T_7 = 70°C)
Source: Created by the authors.

Figure 31, Figure 32 and Figure 33 show the temperature distribution within the heat exchanger. The hot fluid transfers its heat to the walls by convection. Then the heat exchanger walls give this heat to the cold fluid. The hot zones get bigger in the direction the fluid is moving. When the fluid is moving at 1.4 L/min, the temperature change is substantial. The heat exchanger is operating more intensively because the fluid is inside for a longer residence time. At V_h = 2.0 L/min, the temperature is the same everywhere. The heat exchanger makes the temperature of the fluid uniform. The thermal gradient decreases slightly compared to the previous case, indicating a reduction in the heat exchange time. The fluid retains more of its heat due to the higher flow velocity. In the case of Figure 31 with V_h = 2.5 L/min, the temperature contours reveal a more uniform distribution with only a limited axial temperature decrease.

Figure 32 illustrates the evolution and distribution of temperature for a volumetric flow rate V_h of 1.4 L/min. The higher the inlet temperature, the greater the thermal intensity. The thermal gradient remains significant, with progressive cooling of the fluid along the tube. The low flow rate still allows efficient heat exchange. In Figure 32 at V_h = 2.0 L/min, increasing the flow rate produces a more homogeneous thermal distribution along the tube. Elevated temperatures remain present over a larger section of the exchanger, indicating a reduction in heat transfer efficiency due to the shorter fluid residence time within the system. Figure 32 shows the evolution and distribution of the temperature for the case where the volumetric flow rate is the maximum for this type of exchanger (V_h = 2.5 L/min); in this figure, it is clearly visible that the heat distribution is located at the center of the exchanger.

Figure 33 shows how the temperature changes as it flows. This figure uses contours to show how hot or cold the fluid is. The flow rate of the fluid in Figure 33 is still 2.5 L/min. The contours in Figure 33 clearly illustrate what is happening to the temperature of the fluid as it moves. Axial cooling remains visible, with relatively significant heat transfer resulting from the low flow rate and prolonged residence time. For Figure 33 at V_h = 2.0 L/min, the thermal distribution becomes more stable and uniform. Although the temperature decreases progressively, hot regions persist over a longer distance compared to the lower flow-rate case, highlighting the effect of increased flow rate in reducing thermal exchange. Finally, Figure 33 corresponding to V_h=2.5L/min shows temperature contours with only minor variations along the tube length.



V_h = 1.4 [L/min]

V_h = 2.0 [L/min]

V_h = 2.5 [L/min]

Fig. 31: Temperature contour (Case 1: T_7 = 50°C)
Source: Created by the authors.

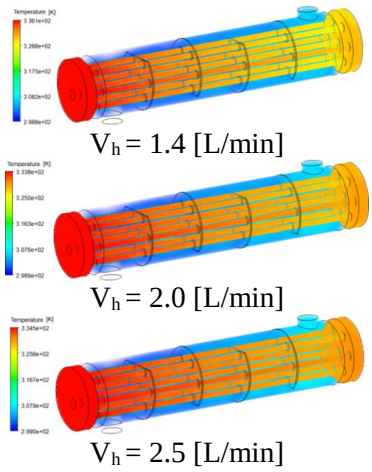


Fig. 32**:** Temperature contour (Case 2: T_7 = 60°C)
Source: Created by the authors.

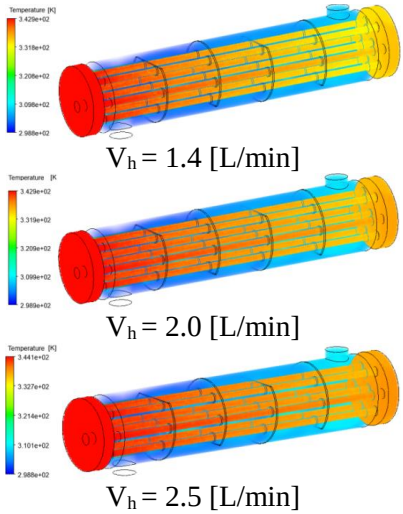


Fig. 33**:** Temperature contour (Case 3: T_7 = 70°C)
Source: Created by the authors.

Figure 34, Figure 35 and Figure 36 illustrate the pressure distributions along the longitudinal section for the nine experimental cases. In Figure 34, for the case of V_h = 1.4 (L/min), the pressure distribution shows a gradual decrease between the inlet and the outlet of the tube. At low flow rates, pressure losses remain limited due to the relatively low fluid velocity. The pressure variation is fairly uniform along the conduit. In Figure 34, for a flow rate of 2.0 L/min, a higher flow rate corresponds to a greater pressure drop. This is because the pressure gradients are more pronounced, indicating pressure losses and friction within the system.

In Figure 34, when the flow rate is 2.5 L/min, the drop in pressure is the biggest. The figures illustrate that the pressure gradually decreases from the inlet to the outlet of the exchanger in the tubes. The losses in pressure are small, which means the flow rate is moderate. For Figure 35, when we increase the flow rate to 2.0 L/min, we see a drop in pressure. The pressure-affected areas shift towards the end of the tube, indicating pressure losses. In Figure 35, with a flow rate of 2.5 L/min, the graph shows that the pressure drops along the pipe. This high flow rate increases friction, thereby increasing pressure loss. Figure 36, with a flow rate of 1.4 L/min, shows that the pressure drops evenly along the pipe. At this flow rate, the fluid is flowing smoothly, which means the losses in pressure are moderate. In Figure 36, for a flow rate of 2.0 L/min, the higher flow rate causes a pressure drop. Finally, Figure 36, for V_h = 2.5 L/min, shows the pressure loss for all cases studied. The pressure declines rapidly along the tube as a consequence of the higher fluid velocity and the increased hydrodynamic resistance within the exchanger.

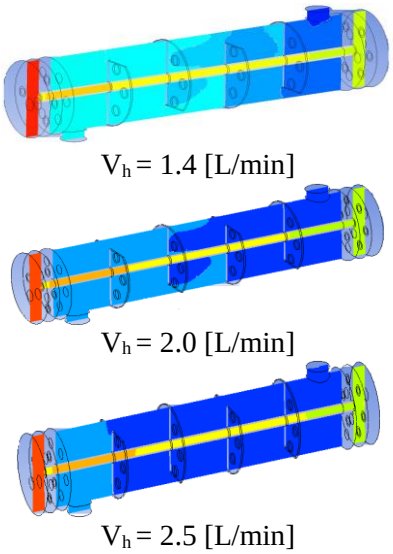


Fig. 34**:** Pressure distribution, Case 1: T_7 = 50°C
Source: Created by the authors.

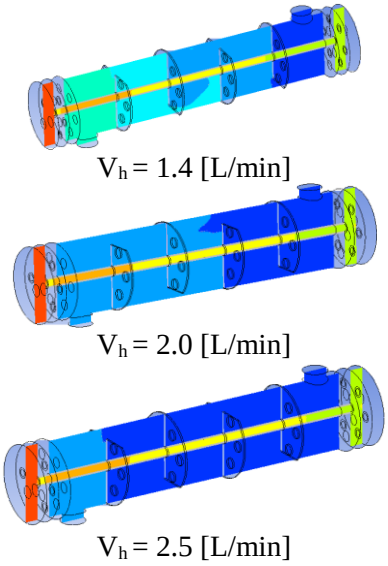


Fig. 35**:** Pressure distribution, Case 2: T_7 = 60°C
Source: Created by the authors.

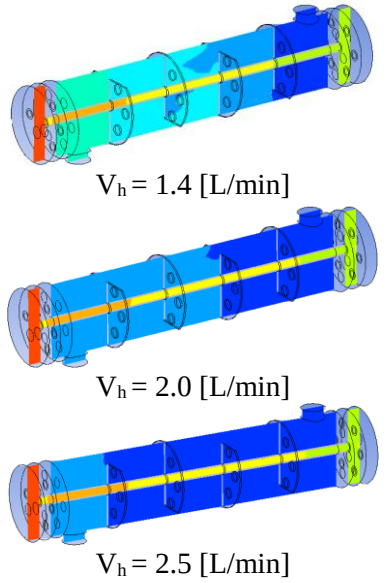


Fig. 36: Pressure distribution, Case 3: T_7 = 70°C
Source: Created by the authors.

5. Conclusion

This study, a practical comparison between experimental calculations and numerical simulation, used a shell-and-tube heat exchanger in a parallel flow configuration. The results indicate that increasing the flow rate improves heat transfer but also increases pressure losses. The good agreement with experimental results confirms the reliability of the model for performance analysis and optimization. In addition, this study presents valuable implications in the field of heat transfer for engineers, enabling them to conduct experiments on test benches and compare the results with those obtained through CFD (Computational Fluid Dynamics). This study demonstrates that the CFD model, once validated, can reliably predict flow behavior, temperature distribution, and heat transfer characteristics.

Declaration of Generative AI and AI-assisted Technologies in the Writing Process

During the preparation of this work, the author(s) utilized artificial intelligence (AI) technologies solely for the purpose of linguistic refinement and grammatical correction. Following the application of these tools, the author(s) comprehensively reviewed, verified, and edited the resulting text. The author(s) maintain full accountability and responsibility for the accuracy, integrity, and final content of the publication.

References:

[1] Almulla, N. M., Moawed, M. A., Abd-Elrahman, M. A., and Salem, M. R., "Study of the thermal performance characteristics of shell and semi-circular tube heat exchangers using both baffles and nanofluid," Engineering Research Journal, Vol. 53, pp. 68–81, 2024, doi: 10.21608/erjsh.2023.243774.1237

[2] Abdelhamid, H. R. M., Bakry, A. I., & Bastawissi H., "A review on comparative performance of shell-and-tube heat exchangers with various design configurations," Journal of Engineering Research, Vol. 6(4). https://jer.journals.ekb.eg/article_502601_28f502c5f082607217be1019e91f82c2.pdf

[3] Abeykoon, C., "Compact heat exchangers: Design and optimization with CFD," International Journal of Heat and Mass Transfer, Vol. 146, Art. No. 118766, 2020, doi: 10.1016/j.ijheatmasstransfer.2019.118766

[4] Chaoui, A., Bouzid, S., Aidi, M., Bordja, L., and Poós, T., "Comparative study of shell-and-tube heat exchanger designs for improved thermal performance and

energy efficiency," Advances in Mechanical Engineering, Vol. 17, No. 12, 2025, doi: 10.1177/16878132251408726

[5] Iqbal, S., Naveed, M. F., Masud, M., Tariq, A., Kausar, T., Nasir, Z., and Babar, M. A., "Experimental evaluation of thermal performance in shell and tube heat exchangers using Al_2O_3-γ nanofluids," Engineering Proceedings, Vol. 75, No. 1, Art. No. 13, 2024, doi: 10.3390/engproc2024075013

[6] Prajapati, P., Raja, B. D., Patel, V., and Jouhara, H., "Energy-economic analysis and optimization of a shell and tube heat exchanger using a multi-objective heat transfer search algorithm," Thermal Science and Engineering Progress, Vol. 56, Art. No. 103021, 2024, doi: 10.1016/j.tsep.2024.103021

[7] Marzouk, S. A., Abou Al-Sood, M. M., El-Said, E. M. S., Younes, M. M., and El-Fakharany, M. K., "A comprehensive review of methods of heat transfer enhancement in shell and tube heat exchangers," Journal of Thermal Analysis and Calorimetry, Vol. 148, pp. 7539–7578, 2023, doi: 10.1007/s10973-023-12265-3

[8] Khan, A., Shah, I., Gul, W., Khan, T. A., Ali, Y., and Masood, S. A., "Numerical and experimental analysis of shell-and-tube heat exchangers with round and hexagonal tubes," Energies, Vol. 16, No. 2, Art. No. 880, 2023, doi: 10.3390/en16020880

[9] Wardhani, A. S. B., Labumay, A. T., and Ningsih, E., "Influence of fluid inflow rate on performance effectiveness of shell and tube type heat exchanger," Journal of Mechanical Engineering, Science, and Innovation, Vol. 2, No. 1, 2022, doi: 10.31284/j.jmesi.2022.v2i1.2993

[10] Khaled, M., Faraj, K., El Hage, H., Faraj, J., Taher, R., and Mortazavi, M., "Multi-passage concept applied to water-air cross flow tubes-and-fins heat exchangers – Thermal modelling and feasibility study," International Journal of Thermofluids, Vol. 17, Art. No. 100291, 2023, doi: 10.1016/j.ijft.2023.100291

[11] ANSYS Inc., ANSYS Fluent Theory Guide. Canonsburg, PA, USA: ANSYS Inc., 2011. https://ansyshelp.ansys.com/public/account/secured?returnurl=/Views/Secured/corp/v251/en/flu_th/flu_th.html?utm_source=chatgpt.com (Accessed: September 23, 2025)

[12] G.U.N.T. Gerätebau GmbH, WL 110-Series Heat Exchanger with Service Unit: Experiment Instructions. Barsbüttel, Germany: G.U.N.T. Gerätebau GmbH, 2010. https://www.gunt.de/en/products/equipment-series/wl-110-series-heat-exchangers (Accessed:November 12, 2025)

[13] Hassan, A. K., Mohaisen, H. S., Mohammed, K. S., Eleiwi, M. A., and Majdi, H. S., "Parametric study of heat transfer in shell and tube heat exchanger: Cooling of engine oil with water and ethylene glycol mixtures," International Journal of Computational Methods and Experimental Measurements, Vol. 13, No. 2, pp. 405–426, 2025, doi: 10.18280/ijcmem.130217

[14] Lee, S., Kim, Y., Choi, A., and Choi, S., "Numerical analysis of heat transfer in a double-pipe heat exchanger for an LPG fuel supply system," Energies, Vol. 18, No. 15, Art. No. 4179, 2025, doi: 10.3390/en18154179

[15] Kalani, I. and Toghraie, D., "Numerical analysis of thermal–hydraulic characteristics and laminar two-phase nanofluid flow inside a tube equipped with helically twisted tapes," Scientific Reports, Vol. 11, Art. No. 12228, 2021, doi: 10.1038/s41598-021-91699-x

[16] ANSYS Inc., ANSYS Gambit Help. Canonsburg, PA, USA: ANSYS Inc., 2011. Available at: https://cfdland.com/ansys-fluent-and-gambit-in-cfd/ (Accessed: September 23, 2025)

[17] Zolfalizadeh, M., Zeinali Heris, S., Pourpasha, H., Mohammadpourfard, M., and Meyer, J. P., "Experimental investigation of the effect of graphene/water nanofluid on the heat transfer of a shell-and-tube heat

exchanger," International Journal of Energy Research, Vol. 2023, Art. No. 3477673, 2023, doi: 10.1155/2023/3477673

[18] Santos Filho, S., Souza, J., and de Lima, A., "Numerical simulation of the shell-and-tube heat exchanger: Influence of the lower flows and the baffles on a fluid dynamics," Advances in Chemical Engineering and Science, Vol. 7, pp. 349–361, 2017, doi: 10.4236/aces.2017.74026

[19] Prończuk, M. and Krzanowska, A., "Experimental investigation of the heat transfer and pressure drop inside tubes and the shell of a minichannel shell and tube type heat exchanger," Energies, Vol. 14, No. 24, Art. No. 8563, 2021, doi: 10.3390/en14248563

[20] Di Bono, G., Corcione, M., and Quintino, A., "Systematic comparative analysis of Kern and Bell-Delaware methods for the design of shell-and-tube heat exchangers," Applied Thermal Engineering, Vol. 278, Part C, No. 127327, 2025, https://doi.org/10.1016/j.applthermaleng.2025.127327

[21] Pérez Sánchez, A., Gómez Julián, A. M., Corpas, N., and Ranero, E., "Thermo-hydraulic rating of a shell and tube heat exchanger for acetone cooling using Bell-Delaware method," Nexo Revista Científica, Vol. 36, No. 4, pp. 524–550, 2023, https://www.camjol.info/index.php/NEXO/article/view/16768/20095

[22] Kern, D. Q., Process Heat Transfer. New York, NY, USA: McGraw-Hill, 1950. https://openlibrary.org/books/OL6070844M/Process_heat_transfer (Accessed: September 10, 2024)

Contribution of Individual Authors to the Creation of a Scientific Article (Ghostwriting Policy)

This research paper is collaborative work. The contribution of each author is outlined below:

Guessab Ahmed: Developed the main idea for the study design, methodology, numerical modeling, data analysis, and manuscript preparation.

Ait Amrane Ouardia: Assisted in developing the simulation model and data analysis.

Finally, all authors reviewed and approved the final manuscript.

Sources of Funding for Research Presented in a Scientific Article or Scientific Article Itself

This research received no external funding. The study was conducted using the resources available to the authors and their affiliated institution.

Conflict of Interest

The authors declare that there is no conflict of interest regarding the publication of this article.

Creative Commons Attribution License 4.0 (Attribution 4.0 International, CC BY 4.0)

This article is published under the terms of the Creative Commons Attribution License 4.0 https://creativecommons.org/licenses/by/4.0/deed.en_US